LAPPEENRANTA UNIVERSITY OF TECHNOLOGY
LUT School of Technology
Computational Engineering

Iurii Kim

FIRST-PRINCIPLES STUDY ON ELECTRONIC AND STRUCTURAL PROPERTIES OF CU(IN/GA)SE ALLOYS FOR SOLAR CELLS

Examiners: Professor Erkki Lähderanta
Professor Martti Puska
Thesis instructor D. Sc. Hannu-Pekka Komsa

ABSTRACT

Lappeenranta University of Technology
LUT School of Technology
Computational Engineering

Iurii Kim

First-principles study on electronic and structural properties of Cu(In/Ga)Se alloys for solar cells

Master's thesis

2015

40 pages, 8 figures and 3 tables

Examiners: Professor Erkki Lähderanta
Professor Martti Puska

Keywords: first-principles, density-functional theory, $CuInSe_2$ alloys, point defects, GGA.

Thin-film photovoltaic solar cells based on the $Cu(In_{1-x}Ga_x)Se_2$ (CIGS) alloys have attracted more and more attention due to their large optical absorption coefficient, long term stability, low cost, and high efficiency. Modern theoretical studies of this material with first-principles calculations can provide accurate description of the electronic structure and yield results in close agreement with experimental values, but takes a large amount of calculation time. In this work, we use first-principles calculations based on the computationally affordable meta-generalized gradient approximation of the density-functional theory to investigate electronic and structural properties of the CIGS alloys. We report on the simulation of the lattice parameters and band gaps, as a function of chemical composition. The obtained results were found to be in a good agreement with the available experimental data.

ACKNOWLEDGEMENTS

The work presented in this thesis has been carried out at the Center of Excellence in Computational Nanoscience (COMP) at the Department of Applied Physics, Aalto University, from December 2014 to June 2015.

I would like to thank my supervisors, Prof. Martti Puska and Prof. Erkki Lähderanta for the opportunity to do my master thesis in the Electronic Properties of Materials group and for the chance to learn this new research area for me. I also want to extend my special thanks to my thesis advisor D. Sc. Hannu-Pekka Komsa for ideas and discussions. Without him this work simply would not have taken place. Finally, I want to thank my family and friends for supporting me despite of borders and distances between us.

Lappeenranta, May 2015
Iurii Kim

ABBREVIATIONS

PV	photovoltaic
CIS	$CuInSe_2$
CIGS	Cu (In, Ga) Se_2
DFT	density-functional theory
ext	external
GGA	generalized-gradient approximation
KS	Kohn-Sham
HF	Hartree–Fock theory
LDA	local-density approximation
xc	exchange-correlation
mBJ	modified Becke and Johnson functional
PBE	Perdew - Burke – Ernzerhof functional
PBEsol	Perdew - Burke – Ernzerhof functional
revTPSS	Tao-Perdew-Staroverov-Scuseria functional
AM05	Armiento – Mattsson functional
cmBJ	c-parameter of modified Becke and Johnson functional
HSE	Heyd, Scuseria, and Ernzerhof functional

TABLE OF CONTENTS

1. INTRODUCTION

One of the greatest challenges of our time is to provide cost-effective and environmentally friendly methods for energy production. Among all the renewable energy sources, photovoltaic (PV) cells have recently seen extremely fast technical development. The first-generation of solar cells used silicon-based materials, including single- and polycrystalline structures, which have now been extensively studied. However, they have disadvantages such as the complex production of pure silicon, which may result in a huge amount of point defects, and the weak light absorption and unsatisfactory conversion efficiency (<25%) for Si-based solar cells [1]. In contrast, a new world record for direct conversion of sunlight into electricity has achieved 46.5% using 4-junction solar cell made of III-V semiconductor materials [2].

Other promising candidates for investigation are ternary materials such as $CuInSe_2$ (CIS) and its alloy $Cu(In,Ga)Se_2$ (CIGS), which has shown good results for applications in the solar cells industry among thin-film materials. Modern research efforts have lead to record efficiency of 21.7%, which shows the important technical potential of CIGS [3]. $CuInSe_2$ has a band gap of 1.04 eV, which is not consistent with the ideal value of 1.40 eV for an absorber of solar light. Other chalcopyrite type compounds, such as $CuGaSe_2$, $CuInS_2$, $CuGaS_2$, exhibit band gaps of 1.68 eV, 1.53 eV, and 2.43 eV, respectively. Therefore, by varying the Ga and In substitution ratio, band gap of the CIGS absorber can be changed from around 1 eV to 2 eV, which can provide high efficiency solar cell [4].

Both experimental and theoretical approaches are helpful to fully describe the electronic structures of CIGS materials and the ensuing implications for solar cells. In laboratory work scientists are often limited in their equipment, for example, in resolution and in controlling the conditions, which makes it challenging to access microscopic details like presence of atomic defects. Hence, computational methods have become increasingly popular to complement experiments. One of these methods is the Density-functional theory (DFT). It is an efficient technique for calculating band gaps, total energies of systems, and other quantities characteristic of the electronic structure. Thus, DFT is very a good instrument for more detailed and accurate studies of materials.

The aim of this work is to investigate electronic and structural properties of $CuInSe_2$ and its alloys using the first-principles DFT method. In particular, we compare different exchange-

correlation functionals in their capability to predict experimental values. Thereby we choose the best method and derive its optimal parameter setting.

The history and the modern progress of solar cells are presented in chapter 2. There we show also the fundamental schemes about the photovoltaic effect, modern manufacturing, and examples of companies in the field of solar batteries. Chapter 3 of this thesis describes the fundamentals of the electronic structure theory, basic knowledge about DFT, modeling of the exchange-correlation energy and the implementation of DFT in practice. Computational details used in this work are described in chapter 4. In chapter 5 we present our results and discuss them.

2. HISTORY AND MODERN PROGRESS IN SOLAR CELLS

In 1839 A.E. Becquerel observed that shining light on certain materials leads creation of electric current. This was the starting point for the photovoltaic technology. Charles Fritts produced in 1883 the world's first solar cell, a device that converts sunlight into electricity, using selenium and gold. The cell's efficiency was less than 1%, meaning than less than 1% of the light energy was converted into electricity. The theoretical foundation for the modern PV technology was laid down by the development of the silicon production technology and by the discovery of the photoelectric effect in 1905 by Albert Einstein. Awarded the Nobel Prize for Physics in 1921, he was the first to postulate the existence of light quanta, photons, thereby providing theoretical foundation for the modern PV technology [5]. In 1954 silicon solar cells started to find their way into the mainstream market. The New York Times wrote that the silicon solar cells could lead to "the harnessing of the almost limitless energy of the sun for the uses of civilization." [6] Soon after, the space race between the U.S. and the Soviet Union starting in 1958 sparked significant investments in the solar technology. Photovoltaic cells provided efficient means to power the satellites, for instance. In 2000 the cumulative global solar installation passed 1 GW, a critical milestone for the whole industry's global development [7]. Solar industry surpassed the computer microchip industry in the consumption of high-purity silicon in 2006. Although a temporary silicon supply shortage was created by this, it also lead to major industrial investments that eventually lowered the price of solar panels. Another important milestone was reached in 2011, when the cost of high-quality silicon solar panels fell to roughly US$1 per watt, proving the economic viability of the technology. Figure 2.1 shows the full range of PV cell types with the world record efficiencies achieved by each year over the past thirty years.

PV is now, after hydro- and wind-powers, the third most important renewable energy source in terms of installed global capacity. The power output of a PV cell or module is rated in peak watts (Wp), meaning the power output at 25°C under the standard AM1.5 (Figure 2.2.) solar radiation of global irradiance 1 kWm^{-2}. AM (Air Mass) is the coefficient denoting the path length which light takes through the atmosphere normalized by the shortest possible path length.

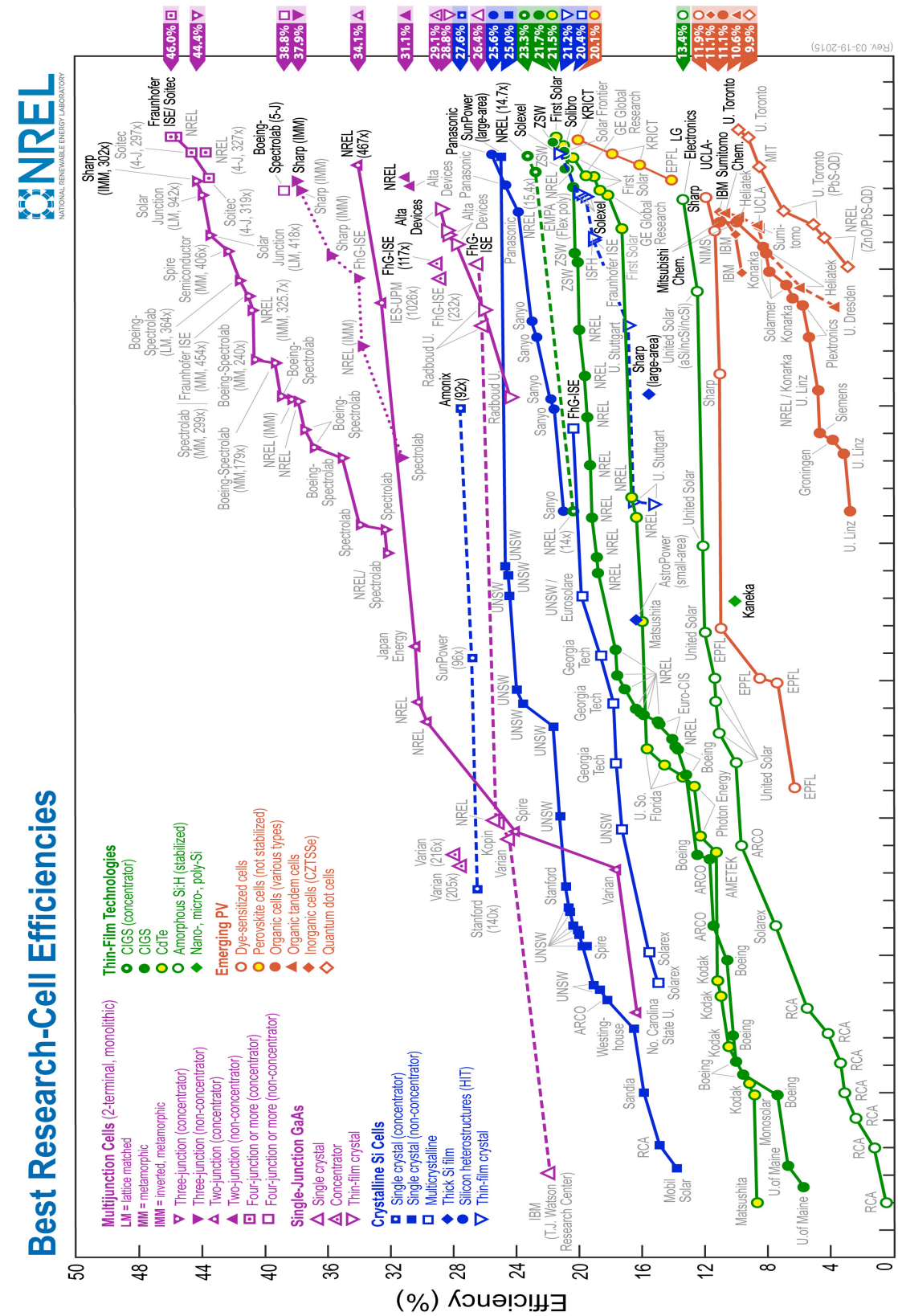

Figure 2.1 Record laboratory cell efficiencies for different PV technologies [8].

The Air Mass quantifies how much the power of light is reduced as it passes through the atmosphere and is subsequently absorbed by air molecules and dust particles. The Air Mass is defined as:

$$AM = \frac{1}{\cos(\theta)}, \tag{1}$$

where θ is the angle from the vertical line (normal to the ground). When the sun is directly overhead, the Air Mass is 1. The standard spectrum at the Earth's surface is called AM1.5G, (G stands for global and includes both the direct and the diffuse radiation) or AM1.5D (which includes direct radiation only).

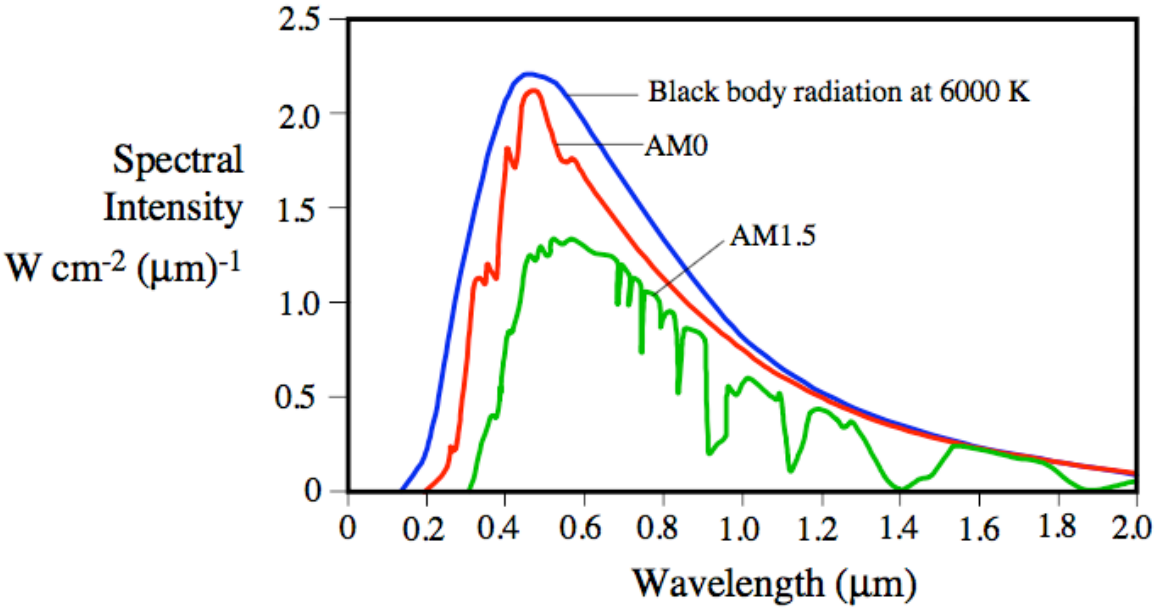

Figure 2.2 The spectrum of the solar energy represented as spectral intensity (I_λ) vs wavelength above the Earth's atmosphere (AM0 radiation) and at the Earth's surface (AM1.5 radiation). Black body radiation at 6000 K is shown for comparison [9].

When PV rating is given in watts it usually means peak watts. Conversion from the peak watt rating to the 24-hour average power output in a sunny location is straightforwardly done simply dividing by a factor of ~5. A standard 156 × 156 mm crystalline silicon PV cell generates about 4 peak watts (Wp) of DC power and typical PV 60-cell and 72-cell modules generates about 240 Wp and 300 Wp respectively. The world's largest PV generating facility

is currently the Agua Caliente Solar Project in Arizona, which had 251.3 MWp installed in November 2013 [10].

The basic schematic description of a typical solar cell is shown in Figure 2.3. Let us consider a pn-junction with a thin and heavily doped n-region. The illumination is through the n-side surface. The depletion region (W) in this case extends mostly to the p-side. In addition, a built-in electric field E_0 is formed inside the depletion layer.

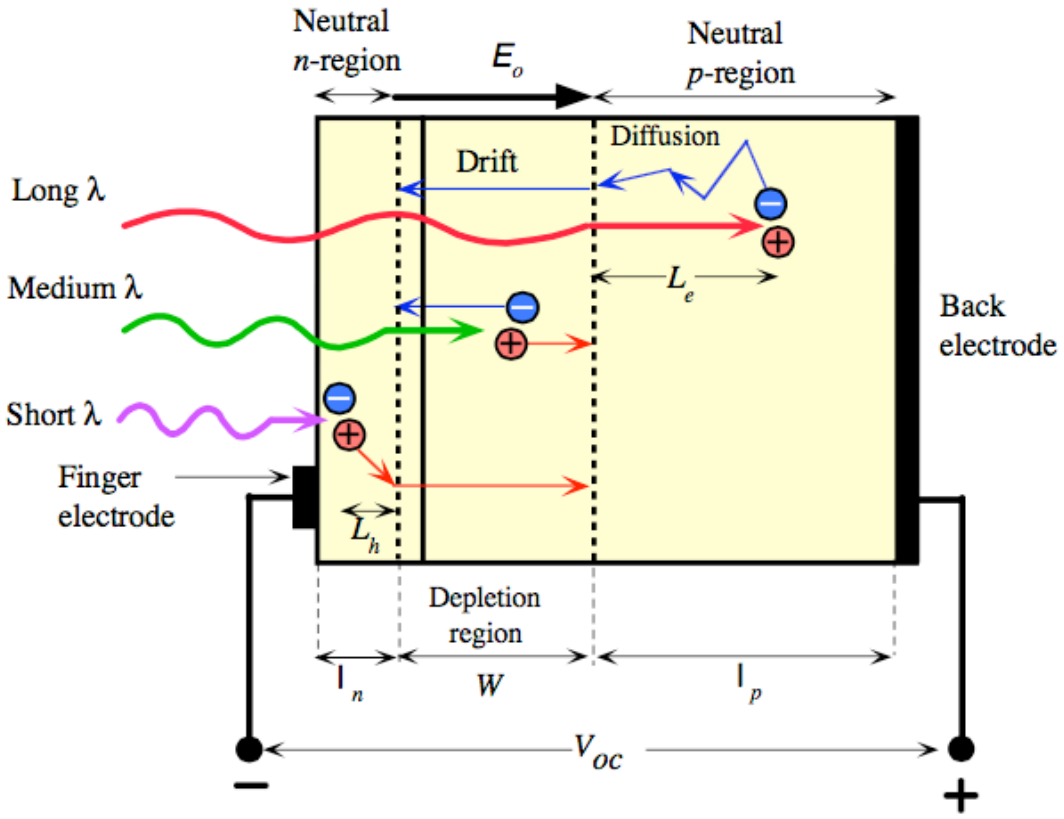

Figure 2.3 The principle of operation of the PV cell [9].

As the n-side is very small, most of the photons are absorbed within the depletion region and within the neutral p-side, where most of the photogenerated electron-hole pairs are formed. These pairs are immediately separated by the built-in electric field E_0. The electron is driven to the neutral n^+ side where it makes this region negative charged. Similarly the holes are driven to the neutral p-side, thereby making this side positive. As a result, an open circuit voltage is created between the two ends of the device with the p-side being positive with respect to the n-side. When external load is connected to the device, the excess electrons from

the n-side can pass through the circuit, performing work, and reach the p-side where they recombine with the excess holes. It is worth noting that the internal field E_0 is critical for separating the photogenerated electron-hole pairs and accumulating excess electrons on the n-side and excess holes to the p-side.

Despite the difficult economic situation, the global PV module production in 2012 was 35.9 GWp [11]. Different scenarios for future trends vary wildly, but the average forecast is about 260 GWp of cumulative installed global PV capacity by 2020. The demand is expected to shift from Europe to developing markets in China, India, but also to USA [12]. In an unstable economic time, many countries including the oil-rich nations are eager to partially move to solar energy to mitigate the effects of crisis. Qatar Solar Technologies made an unprecedented investment of US$ 1 billion in May 2012 to build a polysilicon production facility in Ras Laffan Industrial City. Saudi Arabia aims to meet a third of its electricity with solar power by 2032, while Abu Dhabi has targeted 7% of its power from renewable sources by 2020 and Dubai 5% by 2030 [13].

PV in comparison with the other renewable energy sources eliminates problems such as the service of moving parts, generation emissions, need for cooling (excluding high concentrator systems [14]), short lifespan and complicated use. This present thesis is directly related to one of the most popular types of solar cells, the thin-film. Among all types of solar modules the thin-film modules possess a number of advantages: light weight, low cost, and fabrication as series-connected modules in an integrated manufacturing process. The most widely used thin-film material is cadmium telluride with 46% of the total production among thin-film PV's. On the second place is amorphous/microcrystalline Si with 35%, and next ones are CIS and CIGS (copper indium gallium selenide) with 19% [10].

A number of advantages such as the high efficiency, long-term stable performance and potential for low-cost production make CIS and CIGS of the promising material for thin-film PV technology. Because of the high absorption coefficient ($\sim 10^5$ cm^{-1}) a thin layer of 2 mm is sufficient to absorb the useful part of the spectrum (ideal a-Si has $\sim 10^6$ cm^{-1}) [15]. The highest efficiency achieved for CIGS is 21.7% [3], [16].

One more advantage is that CIS PV independent on the silicon price. For example, the hegemony of wafer-based crystalline Si was challenged in the period 2005-2009 [10] by the

temporary global shortage of Si feedstock. This led to a massive expansion of investments in non-silicon thin-film PV capacity.

Currently, solar cells made from chalcopyrite compound semiconductors are attracting considerable interest for space applications. Proton and electron irradiation tests of CIGS and CdTe solar cells have proven that their stability against particle irradiation is superior to that of Si or III–V solar cells [17]. The low mass, large storage volume, high radiation resistance, and stability of the finished CIS devices also provide a wide range of use in space applications. Recently, the research on low-cost electrodeposition opened a number of advantages over the high-vacuum deposition techniques as a method for PV processing [18]. The new technique allows deposition over large areas at low temperature and atmospheric pressure conditions, and a good control of film thickness. Moreover it is a self-purifying process, allowing the use of low-purity precursor materials. All these features are translated into reduction of production costs.

Microstructural features of the absorber layer, such as types of point defect and their distribution, affect the electronic and structural properties of high-efficiency CIS and CIGS materials [19], [20]. Modern computational methods and the constantly evolving computer technology make it possible to perform accurate computer simulations with predictive power. A very important task is the correct selection of the computational method that is the most suitable for the original problem. Density-functional theory (DFT) calculations have often been used to interpret experimental observations on defects in CIS. For example, using a hybrid functional the energetics of vacancies in $CuInSe_2$ can be calculated in a good agreement with experimental data. It has been also shown, contrary to present beliefs, that copper and indium vacancies induce no defect levels within the band gap and therefore cannot account for any experimentally observed levels [21], [22].

Another example of a successful explanation of the experimental results with DFT calculations are questions involving the role of sodium in $CuInSe_2$. It has been demonstrated that Na reduces the copper mass transport due to the capture of copper vacancies into substitutional Na_{Cu} defects. This finding provides an explanation for experimental measurements where the presence of Na has been observed to decrease copper diffusion [23]. In another case a model of defect-assisted mass transport mechanisms operating in CIS helped

to understand how compositional inhomogeneities arise in CIS. The most mobile species in CIS is shown to be copper, whose migration proceeds either via copper vacancies or interstitials [24].

On the other hand, it is important not to forget the steady experimental progress in understanding electronic structure of chalcopyrites for high-efficiency solar cells [25]. New insights into the dispersion of valence and conduction bands allow to predict the effective masses of charge carriers and their orientational dependence, which influence the charge transport in solar cell absorbers [26], [27].

DFT can be used to give reliable prediction when interpreting experimental observations of atomic-scale phenomena occurring in CIS. Further, it can provide computational insight on defect-related mechanisms that may sometimes remain out of reach in experiments.

3. FIRST PRINCIPLES METHODS IN MATERIALS MODELLING

3.1. Electronic structure theory

In order to study electronic and structural properties of any material we must start by describing the many-body system of interacting electrons and nuclei. The many-body theory is based on the Schrödinger equation with the Hamiltonian

$$\hat{\mathrm{H}} = -\frac{\hbar^2}{2m_e}\sum_i \nabla_i^2 - \sum_{i,I}\frac{Z_I e^2}{|r_i - R_I|} + \frac{1}{2}\sum_{i\neq j}\frac{e^2}{|r_i - r_j|} - \sum_I \frac{\hbar^2}{2M_I}\nabla_I^2 + \frac{1}{2}\sum_{I\neq J}\frac{Z_I Z_J e^2}{|R_I - R_J|}, \qquad (2)$$

where electrons and nuclei are denoted by lower- and upper-case subscripts, respectively. Z and M are the charge and the mass of the nuclei, respectively. To make the understanding simpler, equation (2) is written without magnetic fields, relativistic effects and quantum electrodynamics ([28], chapter 3).

Assuming that the nuclei of the material are spatially fixed, which can be justified by their high mass in comparison to that of electrons, it is possible to say that the nuclear kinetic energy is fixed. Then, the fundamental Hamiltonian for the theory of the electronic structure can be written as

$$\hat{\mathrm{H}} = \hat{\mathrm{T}} + \hat{\mathrm{V}}_{ext} + \hat{\mathrm{V}}_{int} + E_{II}\,. \qquad (3)$$

This approximation is called as the Born-Oppenheimer approximation. The Hamiltonian consists of the kinetic energy operator T for the electrons, external potential V_{ext} acting on electrons due to the nuclei, Coulombic electron-electron interaction $V_{int,}$ and interaction E_{II} between the nuclei. The adoption of the Hartree atomic units, by defining $\hbar=m_e=e=4\pi/\varepsilon_0=1$, makes it possible to write the operators in (3) as:

$$\hat{\mathrm{T}} = \sum_i -\frac{1}{2}\hat{\nabla}_i^2\,, \qquad (3)$$

$$\hat{\mathrm{V}}_{ext} = \sum_{i,I}\mathrm{V}_I(|r_i - R_I|)\,, \qquad (4)$$

$$\hat{\mathrm{V}}_{int} = \frac{1}{2}\sum_{i\neq j}\frac{1}{|r_i - r_j|}\,. \qquad (5)$$

The last symbol in (3), $E_{II,}$ is the classical interaction between nuclei or any other terms that facilitate the total energy of the system and also other external potentials, such as an electric field or the Zeeman effect ([28] chapter 3).

Other important quantities, which play core roles in the electronic structure theory, are the density of particles *n(r)* and the total energy *E* of the system. Using the expectation value of the density operator, *n(r)* can be written as

$$n(r) = \frac{\langle \Psi | \hat{n}(r) | \Psi \rangle}{\langle \Psi | \Psi \rangle} = N \frac{\int d^3 r_2 .. d^3 r_N \sum_{\sigma_1} |\Psi(r, r_2, r_3 ..., r_N)|^2}{\int d^3 r_1 d^3 r_2 .. d^3 r_N |\Psi(r, r_2, r_3 ..., r_N)|^2} . \quad (6)$$

The total energy is given by expectation value of Hamiltonian:

$$E = \frac{\langle \Psi | \hat{H} | \Psi \rangle}{\langle \Psi | \Psi \rangle} = \langle \hat{H} \rangle = \langle \hat{T} \rangle + \langle \hat{V}_{int} \rangle + \int d^3 r V_{ext}(r) n(r) + E_{II} . \quad (7)$$

3.2. Basics of the density-functional theory

The core idea of the density-functional theory (DFT) is that all the information about the system in question is in the electronic density *n(r)*. In other words, any property of an atomic system can be shown in terms of the electronic density, which depends on only three coordinates, instead of wavefunctions with *3N* degrees of freedom [29].

The basis of DFT was laid in two theorems first proved by Kohn and Hohenberg [30] for spin-paired systems and later formulated for the spin-polarized case [31]. The theorems state that the ground-state particle density of the system, n(r), is determined by the external potential V_{ext}. In accordance with the axioms of quantum mechanics the many-body wave function ψ, as well as *n(r)*, contain all the information about the system. Moreover, there exist a functional of the density $E[n_\uparrow, n_\downarrow]$ ($n_\uparrow$, $n_\downarrow$ are the spin-up and spin-down densities, respectively), valid for any external potential V_{ext}, whose global minimum value is the exact ground state energy E_0 and the corresponding density is the exact ground state energy *n(r)*. Thus, the functional $E[n_\uparrow, n_\downarrow]$ is enough to determine all the properties of the system ([28], chapter 6).

However, the proofs of the Hohenberg-Kohn theorems do not provide means for constructing the functional $E[n_\uparrow, n_\downarrow]$. The practical approach of the DFT theory based on an auxiliary independent-particle system was introduced by Kohn and Sham [32]. By

construction, the Kohn-Sham system is supposed to have the same ground state density as the original many-body system. The Kohn-Sham system is described by an independent particle Schrödinger like equation

$$h^{KS}\psi_{i\sigma}(r) = \varepsilon_{i\sigma}\psi_{i\sigma}(r), \tag{8}$$

which defines the Kohn-Sham wave functions $\psi_{i\sigma}$ and eigenenergies $\varepsilon_{i\sigma}$. The effective Kohn-Sham Hamiltonian is

$$\mathrm{H}^{KS} = \underbrace{-\frac{1}{2}\nabla^2}_{t^{KS}} + \underbrace{\mathrm{V}^{H}[n](r) + \mathrm{V}_{\sigma}^{ext}(r) + \mathrm{V}_{\sigma}^{xc}[n_{\uparrow}, n_{\downarrow}](r)}_{\mathrm{V}_{\sigma}^{KS}[n_{\uparrow}, n_{\downarrow}](r)}, \tag{9}$$

which contains explicitly the independent-particle kinetic energy t^{KS} and the long-range Hartree potential V^H corresponding to the classical Coulomb interaction energy. The single-particle external potential is the same as in the original system, i.e. V^{ext} in (3) and (4). The exchange-correlation potential $V^{XC}[\mathrm{n}_{\uparrow}, \mathrm{n}_{\downarrow}]$ is defined to contain all the missing many-body aspects of the original system. By the Hohenberg-Kohn theorems applied to the non-interacting Kohn-Sham system, the exchange-correlation potential V^{XC} is in principle a functional of the spin-dependent density $n_\sigma(r)$ alone ([28], chapter 7).

The Kohn-Sham Hamiltonian (9) depends on the solutions $\psi_{i\sigma}$ through the density

$$n_{\sigma}(r) = \sum_{i} f_{i\sigma} \left|\psi_{i\sigma}(r)\right|^2, \tag{10}$$

whence the equations (8) and (9) have to be iterated to obtain a self-consistent solution. Once the self-consistency is achieved, the ground state electron density is given by (10) ([28], chapter 7).

By definition, it is clear that it is not straightforward to write down the exact form for the exchange-correlation potential $V^{XC}[n_{\uparrow}, n_{\downarrow}]$. However, if it were known, or a suitable approximation to it is at hand, the independent-particle Kohn-Sham wave functions $\psi_{i\sigma}$ could be solved from (9). The ground state is obtained by assigning the $N=N_{\uparrow}+N_{\downarrow}$ electrons to the N_σ lowest orbitals $\psi_{i\sigma}$ in energy $\varepsilon_{i\sigma}$ for both spins $\sigma \in \{\uparrow,\downarrow\}$, yielding the occupation numbers $f_{i\sigma}$. When the external potential $V^{ext}(r)$ is independent of the spin σ, one may consider the spin channels to be paired in spin-degenerate systems. Then the calculations include only one spin channel, say $\sigma = \updownarrow$, and the occupation numbers $f_{i\sigma}$ are typically 2. However, the spin-paired

approach is not valid for, e.g., magnetic systems where the spin-degeneracy is lifted ([28], chapter 7).

In fact, only the total energy and density obtained from the Kohn-Sham formalism are physically meaningful quantities [28]. While, in principle, DFT could provide an exact description of the ground state of the system, in practice, its implementation within the Kohn-Sham formalism is limited by the accuracy of the approximation used for the exchange-correlation functional.

The Kohn-Sham approach presents two clear advantages. First, the interacting many-body problem is reduced to a much more tractable set of independent-particles equations. Second, by explicitly separating out the independent-particle kinetic energy and the long range Hartree terms, it turns out that the remaining exchange-correlation functional $E_{xc}[n]$ can be reasonably well approximated using a (semi-)local functional of the density. Even though the exact functional $E_{xc}[n]$ is not known and is practical situations likely very complex, great progress has been made in developing simple approximations that still work well.

3.3. Modeling the exchange-correlation energy

The crucial quantity in the Kohn-Sham approach is the exchange-correlation energy $E_{xc}[n]$ which is expressed as a functional of the density. As it says in the name, the exchange-correlation interaction between electrons consists of two contributions: exchange and correlation. Exchange arises from the Pauli exclusion principle according to which any two electrons cannot occupy the same quantum-mechanical state. Correlation encompasses screening effects of electrons, whereby electrons collectively correlate to reduce the net interaction between any two electrons. Capturing these effects within some approximation in a satisfactory way has been a longstanding problem within the DFT community [28].

Already in their seminal paper, Kohn and Sham realized that solids could often be considered as being similar to the homogeneous electron gas. Indeed, the resulting local-density approximation (LDA) is the simplest and one of the most widely used approximations for the exchange-correlation energy. LDA is based on the observation that valence electron densities typically found in solids resemble that of a homogeneous electron gas, where the range of the effects of exchange and correlation is rather short. Therefore, E_{xc} can be approximated locally as the energy of a homogeneous electron gas with the same density n.

LDA has been found to provide surprisingly accurate predictions for experimental results on a wide range of materials, though it shows a clear preference for systems with slowly varying electron densities. Delocalizing electronic densities causes excessive bonding in atomic systems, leading to an overestimation of binding energies and underestimation of bond lengths. Systems lying completely beyond the reach of LDA are those that do not resemble non-interacting electron gases, such as strongly correlated materials [33], [34].

The following approximations are essentially improvements and extensions of LDA. The success of the LDA has led to developing extensions, which include density gradients in various generalized-gradient approximations (GGAs) and yield results in marked improvement over LDA in many cases. Widely used GGAs can in some instances provide sufficient accuracy for DFT to be widely adopted by the chemistry community. The basic problem is that in real materials density gradients can be so large that the gradient expansion is no longer valid.

For different materials and problems there are many functionals, among which the most used ones are the Perdew – Burke - Ernzerhof (PBE [35]), Armiento - Mattsson (AM05 [36]) and Perdew – Burke - Ernzerhof revised for solids (PBEsol [37]) functionals.

The functionals can be further improved by adding to it more (local) information about the system. A meta-GGA DFT functional in its original form includes the second derivative of the electron density (the Laplacian) whereas GGA includes only the density and its first derivative in the exchange-correlation potential [38]. Functionals of this type are, for example, the Tao-Perdew-Staroverov-Scuseria (TPSS [39]), its revised version revTPSS [39], and modified Becke and Johnson (mBJ [40]) functionals.

Generalized-gradient, or in other words (semi-)local approximations, have some deficiencies such as the presence of the self-interaction. It is means that each electron interacts also with itself through the effective potential. These shortcomings lead, for instance, to an unphysical delocalization of localized states and an underestimation of band gaps [41]. Including a component of the exact exchange energy calculated from the Hartree–Fock (HF) theory, can solve most of these difficulties. Functionals of this type are known as hybrid functionals [42], [43]. In the Hartree-Fock approach, the many-electron wavefunction include a behavior of orbitals that leads to cancelling the electron self-interaction.

A hybrid exchange-correlation functional is usually constructed from a portion of exact exchange from the Hartree-Fock theory and correlation from a GGA-type PBE functional:

$$E_{xc}^{hybrid} = \alpha E_x^{HF} + (1-\alpha) E_x^{PBE-GGA} + E_c^{PBE-GGA}, \quad (11)$$

where x denotes exchange and c denotes correlation. The fraction of exact exchange, α, can in principle be tuned, although its default value of 0.25 has been derived from the perturbation theory. Computing the Hartree-Fock part is typically one order of magnitude more expensive than using PBE-GGA for exchange due to necessity to sum over states and k-points. [29]

A further improved version of hybrid functionals takes into account the fact that electron-electron interactions are screened off at longer distances in extended systems. The non-local exchange is therefore separated into two parts – long-range and short-range – and only the latter is treated with the Hartree-Fock theory, reducing the computational time. The most common exchange-correlation energy functional for solid-state systems was proposed by Heyd, Scuseria, and Ernzerhof (HSE) [44].

In this work we use different LDA, GGA and meta-GGA functionals and compare their results to those from the more accurate HSE method, which is computationally heavy. The block diagram (Figure 3.1) demonstrates various approximations and scale of its descriptions.

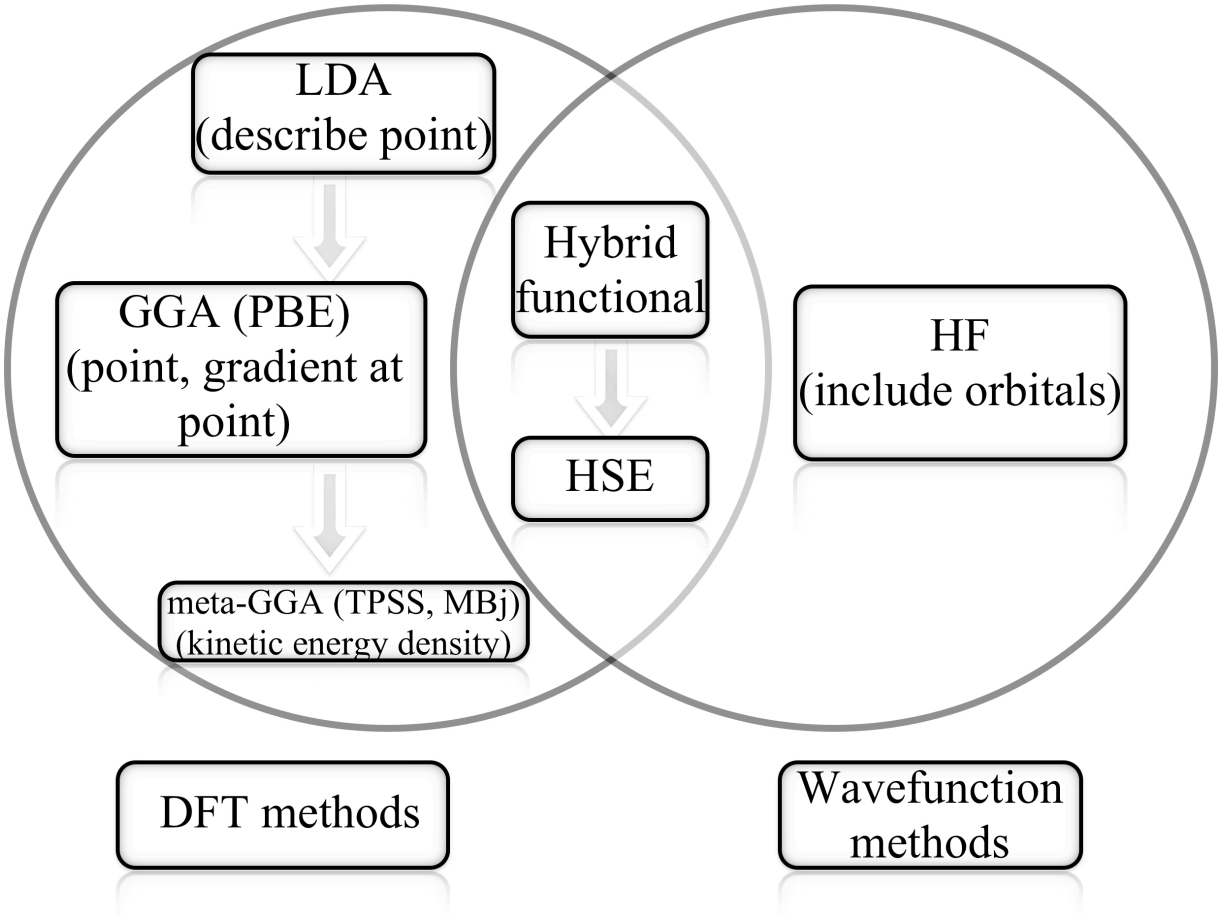

Figure 3.1 Various methods of approximating electronic structure calculations. The constraints of each approximation are given in parentheses. Thus, LDA describes only the local-point effects of the density, in GGA the density gradient at the given point is added, and in meta-GGA the local kinetic energy and density are used as the arguments.

3.4. Implementation of the density-functional theory in practice

The objective of the most ab-initio (or first-principles) approaches based on fundamental quantum theory is to calculate stationary states of electrons in the electrostatic field of atomic nuclei, i.e., the electronic structure. The energy of this ground state can then serve as the basis for investigating displacements of the nuclei, which leads to the determination of many macroscopic properties. DFT was invented to include correlation effects without using the very costly wavefunction methods. Nowadays, most ab-initio methods used in materials science and solid-state physics are based on DFT.

The main advantage of the ab-initio approach is its independence on experimental data. In contrast to semi-empirical methods, there is no need for the calibration or fitting parameters. Thus, ab initio methods can also be used for calculations of some structural and mechanical characteristics of hypothetical systems, i.e., for prediction of properties of materials that have not yet been developed. [45]

Plane waves and real-space grids provide common methodologies for the solution of differential equations such as the Schrödinger and Poisson equations. On the one hand, these methods are different. On the other hand, they are two sides of the same coin. Plane waves are especially suitable for periodic crystals where they provide intuitive understanding as well as simple algorithms for practical calculations. The number of plane waves employed in the calculations usually is determined by setting a cutoff energy to their kinetic energies. Methods based on real-space grids are most appropriate for finite systems and are prevalent in many fields of science and engineering. Usually the two schemes are introduced together because modern electronic structure algorithms use both plane waves and grids with fast Fourier transforms: The kinetic and the exchange-correlation energy functionals are calculated in the diagonal plane-wave and real-space representations, respectively. [28]

Very important concept in electronic structure calculations is “pseudopotential”. The core idea in this approach is to replace the strong Coulomb potential of the nucleus and the effects of the tightly bound core electrons by an effective ionic potential acting on the valence electrons. Such pseudopotentials can be generated through accurate calculations for isolated atoms, and then used to more efficiently calculate various properties of molecules or solids, which are often dominated by the valence electrons. These pseudopotentials are not unique, which allows one to do tradeoffs between their accuracy and computational efficiency. The invention of “ab initio norm-conserving” and “ultrasoft” pseudopotentials led to accurate calculations that are used in much of the current computational research.

One of the pseudopotentials goals is to create pseudofunction that are as “smooth” as possible, and of course are accurate. One meaningful definition of maximizing “smoothness” is to minimize the number of basis functions needed to describe the valence properties to a given accuracy. “Norm-conserving” pseudopotentials achieve the goal of accuracy, usually at some sacrifice of “smoothness”.

In this work, the projector-augmented-wave (PAW) method has been employed, that uses pseudopotential operators but keeps the full core wave functions. The PAW approach also defines a functional for efficient solution of the generalized eigenvalue problem. However, the difference is that the PAW approach keeps the full all-electron wavefunction, since the full wavefunction varies rapidly near the nucleus, all integrals are evaluated as a combination of integrals of smooth functions extending throughout space plus localized contributions evaluated by radial integration over muffin-tin spheres.

4. COMPUTATIONAL METHODS

4.1. Crystal structures of chalcopyrite compounds

$CuInSe_2$ belongs to the group of ternary chalcopyrite compounds, which can be derived from the group IV class of tetrahedral bonded semiconductors according to the Grimm-Sommerfeld rule, i.e., there must be on the average 4 valence atoms per atomic site. In these structures each atom has four neighbors located at the corners of a regular tetrahedron bonded by sp^3 orbitals. The tetrahedral structure of the chalcopyrite can be considered as a superlattice of the sphalerite or zincblende (ZnS) structures. These two lattices have diamond structure (such as silicon or germanium), which is composed of two inter-penetrating face centered cubic lattices, separated by the translation vector of $(\frac{1}{4},\frac{1}{4},\frac{1}{4})a$ (a is a cubic lattice constant), where one sublattice is filled by cations and the other by anions (II-VI and III-V compounds). In ternary chalcopyrite the cations are furthermore replaced by one cation of higher valence and one cation of lower valence which occupy the cation sublattice in an ordered manner as shown in Figure 4.1. In this case, $CuInSe_2$ can be considered as the ternary analogue of the binary ZnS. The reduced symmetry, due to the two kinds of cations, leads to a primitive cell of eight atoms in the chalcopyrite structure compared to a primitive cell of two atoms in the zincblende structure. The Bravais lattice of the chalcopyrite is body centered tetragonal. Compared to the face centered cubic Bravais-cell of the zincblende the unit cell is doubled along the crystal c axis. If different cations are distributed at random, the ternary compound has a sphalerite structure [46] [47].

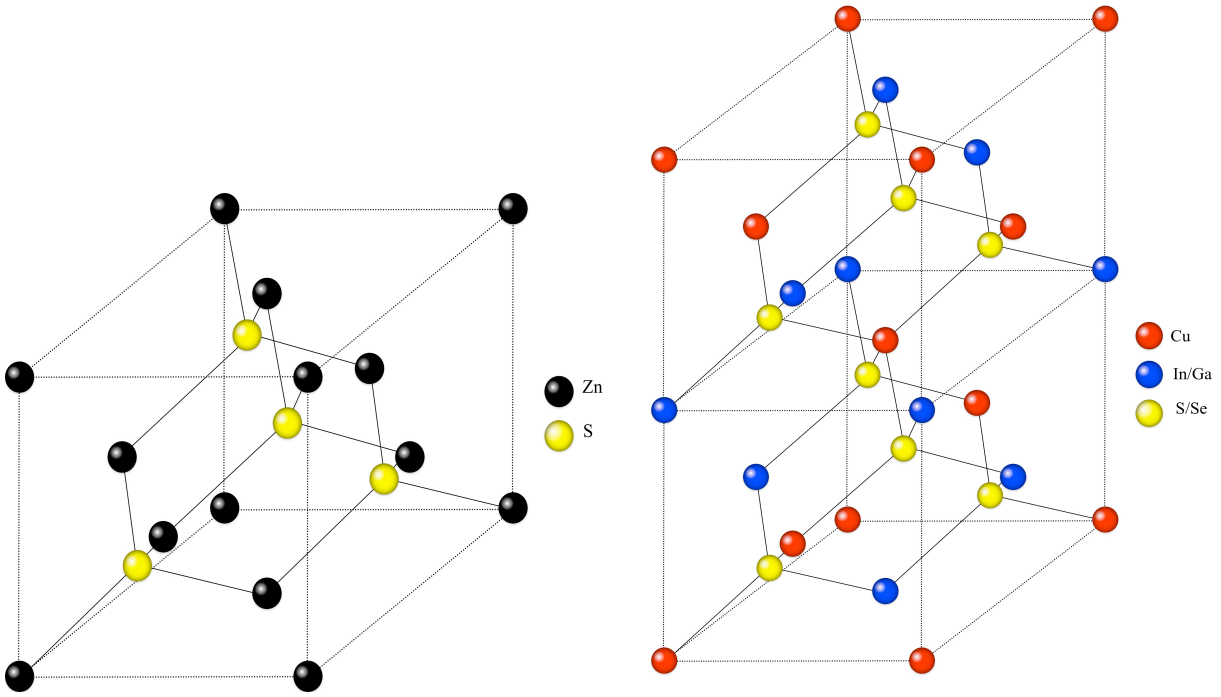

Figure 4.1 Crystal structure of zincblende (left) and chalcopyrite lattice (right).

4.2. Electronic structure of alloys computational details

In this work, we consider ternary compounds with 16 atoms in the unit cell. The lattice constant a corresponds to the lattice constant of the tetragonal chalcopyrite structure. The (c/a) ratio and the internal displacement parameter (u) reveal the distortion of the anion sublattice due to different surroundings. In the ideal structure, c/a =2 and u = 1/4. The lattice constants are optimized together with relaxation of the atomic positions to obtain the equilibrium structural parameters.

All calculations are carried out using the Vienna ab-initio simulation package (VASP) with a plane-wave basis set. The optimization of the lattice parameters and the relaxation of the atomic positions is done using the residual minimization scheme, direct inversion in the iterative subspace (RMM-DIIS). The atomic relaxation is stopped when forces acting on atoms are less than 0.01 eV/Å. The energy cutoff was set to 400 eV, and 3×6×6 grid of Monkhorst-Pack k-points was found to yield converged energies. Exchange and correlation potentials are included using several forms: LDA, GGA (PBE, PBEsol and AM05), and meta-GGA (revTPSS and mBJ).

Band gaps of chalcopyrite compounds were calculated by the same LDA and GGA methods. In this case, the self-consistent procedure is performed on the 3×6×6 grid of Gamma-points uniformly distributed in the irreducible part of the body-centered Brilloin zone (BZ) with the same 400 eV cutoff energy. A further increase in the cutoff value and the number of k-point did not lead to significant changes in the eigenvalues. In addition to calculating band gaps using the same functionals as for relaxation process, we also employ the mBJ functional on top of the revTPSS structure, which has proven to be an efficient approach for accurately determining the fundamental band gaps.

To study the $CuGa_xIn_{1-x}Se_2$ alloy we construct cubic 64 atom supercells of the zinc-blende structure. $CuGa_xIn_{1-x}Se_2$ alloy structures with Ga concentrations between $0 \le x \le 1$, with x = {0, 25, 50, 75, 100}%, are investigated. The initial lattice constants are interpolated using the Vegard's rule [48]

$$\alpha_{Ga_xIn_{1-x}} = x\alpha_{Ga} + (1-x)\alpha_{In}. \tag{12}$$

Also for this calculation we set cutoff energy 400 eV.

In this work, we also used a simple modification of the original Becke and Johnson (BJ) exchange potential, which yields band gaps with accuracy comparable to approaches that are orders of magnitude more expensive. The modified BJ potential (mBJ), which we used, is

$$v_{x,\sigma}^{\mathrm{MBJ}}(\mathrm{r}) = cv_{x,\sigma}^{\mathrm{BR}}(\mathrm{r}) + (3c-2)\frac{1}{\pi}\sqrt{\frac{5}{12}}\sqrt{\frac{2t_\sigma(\mathrm{r})}{\rho_\sigma(\mathrm{r})}}, \tag{13}$$

where $\rho_\sigma = \sum_{i=1}^{N_\sigma} |\psi_{i,\sigma}|^2$ is the electron density, $t_\sigma = \frac{1}{2}\sum_{i=1}^{N_\sigma} \psi_{i,\sigma}^* \cdot \nabla\psi_{i,\sigma}$ is the kinetic-energy density, and

$$v_{x,\sigma}^{\mathrm{BR}}(\mathrm{r}) = -\frac{1}{b_\sigma(\mathrm{r})}(1 - e^{-x_\sigma(\mathrm{r})} - \frac{1}{2}x_\sigma(\mathrm{r})e^{-x_\sigma(\mathrm{r})}) \tag{14}$$

is the Becke-Roussel (BR) [49] potential which was proposed to model the Coulomb potential created by the exchange hole. x_σ is determined from an question involving ρ_σ, $\nabla\rho_\sigma$, $\nabla^2\rho_\sigma$, and t_σ and then b_σ is calculated with $b_\sigma = [\frac{x_\sigma^3 e^{-x_\sigma}}{8\pi\rho_\sigma}]^{\frac{1}{3}}$. In Equation 13, c-parameter was chosen to depend linearly on the square root of the average of $|\nabla\rho|/\rho$:

$$c = \alpha + \beta\left(\frac{1}{V_{cell}}\int_{cell}\frac{\nabla\rho(\mathrm{r}')}{\rho(\mathrm{r}')}d^3r'\right)^{\frac{1}{2}} \quad (15)$$

where α and β are two free parameters and V_{cell} is the unit cell volume [50].

In the VASP implementation of the mBJ potential, the c-parameter (or cmBJ) can be either determined self-consistently or fixed by the user [51]. The latter approach is chosen here and the optimal cmBJ parameter is determined by calculating the band gaps of parental CuInSe and CuGaSe compounds and by comparing them to the experimental values (Tables 5.2 and 5.3). The mean value for the $CuGa_xIn_{1-x}Se_2$ was calculated from the best matches of theses tables. All the structural parameters of the compounds used in this work are fully optimized upon VASP.

5. RESULTS AND DISCUSSION

5.1. Comparison of results obtained by GGA and meta-GGA methods

The results of the lattice structure optimization of chalcopyrite compounds are summarized in Table 5.1. The experimental lattice constants and distortion parameter u are taken from the Landolt-Bornstein tables [52].

Usually LDA underestimates and PBE overestimates lattice constants (and the cell volume), which is also largely true in our case. The difference between theoretical and experimental *c*/*a* ratio on the other hand is very small, less than 1%.

Table 5.1 Experimental [52] and theoretical (LDA, GGA, and meta-GGA) lattice constants, c/a ratio, and distortion parameter u for chalcopyrite compounds.

	$CuGaS_2$				$CuGaSe_2$			
	a, Å	*c,* Å	*c/a,* Å	*u,* Å	*a,* Å	*c,* Å	*c/a,* Å	*u,* Å
Exp.	5.350	10.460	1.955	0.251	5.610	11.000	1.961	0.247
LDA	5.240	10.426	1.990	0.242	5.515	10.980	1.991	0.240
GGA (PBE)	5.386	10.674	1.982	0.247	5.681	11.276	1.985	0.243
GGA (PBEsol)	5.296	10.526	1.987	0.243	5.577	11.095	1.990	0.241
meta-GGA (AMO5)	5.311	10.547	1.986	0.244	5.596	11.124	1.988	0.242
meta-GGA (revTPSS)	5.347	10.582	1.979	0.247	5.607	11.123	1.984	0.244

	$CuInS_2$				$CuInSe_2$			
	a, Å	*c,* Å	*c/a,* Å	*u,* Å	*a,* Å	*c,* Å	*c/a,* Å	*u,* Å
Experimental	5.520	11.080	2.007	0.223	5.780	11.550	1.998	0.220
LDA	5.448	10.960	2.012	0.213	5.715	11.496	2.012	0.213
GGA (PBE)	5.587	11.258	2.015	0.218	5.881	11.843	2.014	0.217
GGA (PBEsol)	5.511	11.105	2.015	0.214	5.783	11.625	2.010	0.214
meta-GGA (AMO5)	5.517	11.097	2.011	0.215	5.781	11.623	2.011	0.215
meta-GGA (revTPSS)	5.541	11.196	2.020	0.217	5.799	11.669	2.012	0.216

For lattice constant, deviation between theory and experiment less than 1-2% is considered good achievement with the current functionals [53]. It is necessary to note that LDA give close values of lattice constant *c* for gallium materials, AM05 vice versa for indium. However, when considering all materials and all lattice parameters, the closest to the experimental are only PBEsol and revTPSS methods.

The band gaps E_g of chalcopyrite compounds calculated using different functionals in comparison with available experimental data are presented in Table 5.2. The experimental band gaps are taken from the Landolt-Bornstein tables.

Table 5.2 The experimental energy [52] band gaps E_g compared to theoretical GGA and meta-GGA approximations of chalcopyrite compounds. In empty places the obtained values for band gaps were very close to zero.

	$CuGaS_2$	$CuGaSe_2$	$CuInS_2$	$CuInSe_2$
E_g Experimental, eV	2.43	1.68-1.96	1.53	1.0-1.3
E_g LDA, eV	0.9	0.2	~	~
E_g GGA (PBE), eV	0.63	~	0.01	~
E_g GGA (PBEsol), eV	0.75	0.12	~	~
E_g meta-GGA (AMO5), eV	0.81	0.18	0.01	~
E_g meta-GGA (revTPSS), eV	0.8	0.27	0.01	0.01
E_g mBJ, eV	1.5	0.99	0.57	0.38

As shown in the table, the obtained values for materials with experimentally small band gap are zero or trends to zero. On the other hand, for the experimentally wide-gap materials, the computational band gap becomes larger than zero, but is still significantly underestimated.

In any case, unfortunately, in the current form all the methods excluding mBJ demonstrate a more than 70% difference with the experiment values, which proves absolutely useless for the band gap analysis. Regarding to mBJ, the difference is less than 50% (for example for $CuGaSe_2$ or $CuGaS_2$) thus making it the best method in our calculations, but still leaving room for improvement. As mentioned earlier, when using the mBJ potential, the VASP software allows to set the *c*-parameter (Eq. 15) by our selves or to calculate it self-consistently. In this section, the cmBJ parameter has been set to the default (1.2662 for $CuInSe_2$ and 1.2692 for $CuGaSe_2$), but by changing the parameter much improved results can be obtained, as will be shown in section 5.3.

5.2. Dependence of the lattice constant on the concentration of the Ga/In

As it was mentioned above, revTPSS and PBEsol are the most accurate methods, which shows the closest values to experimental data according to the table 5.1. Thus, in the following, they have been chosen for the further study of alloy properties.

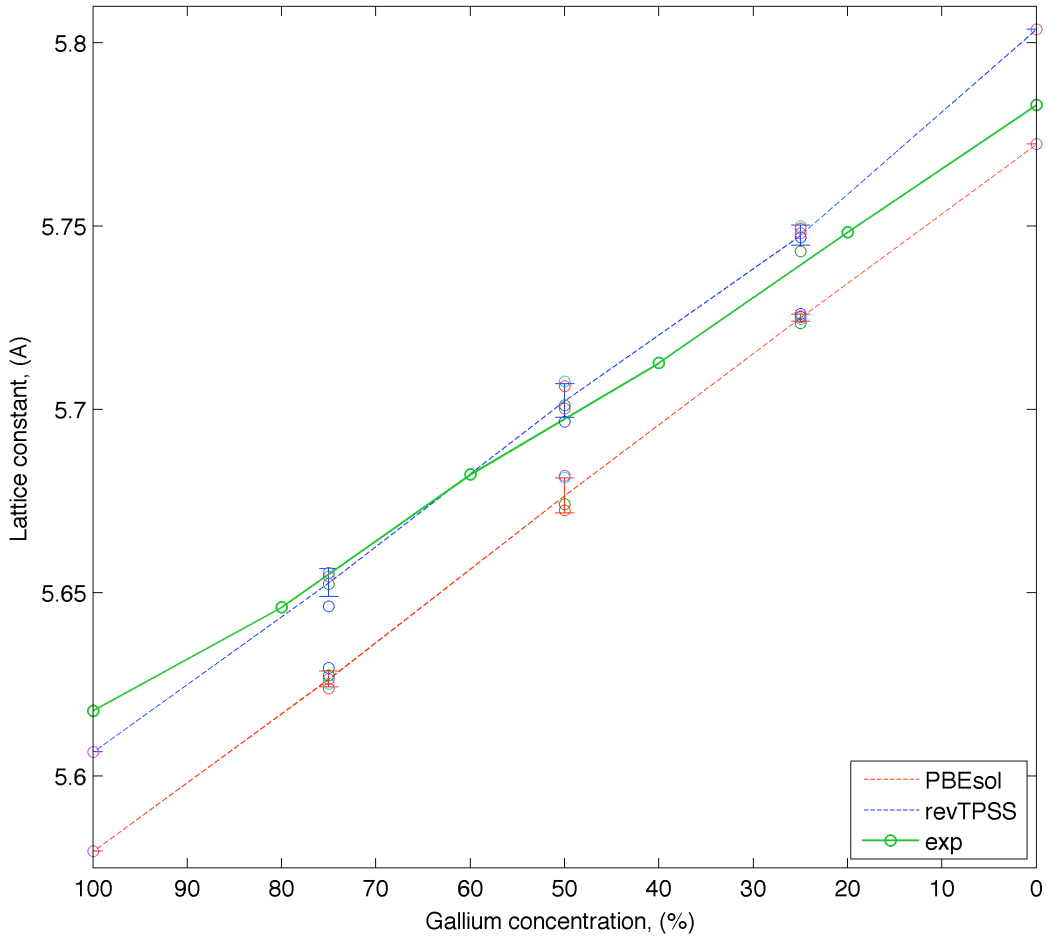

Figure 5.1 Dependence of lattice constant *a* on gallium concentration with different random atomic positions (circles) obtained by PBEsol and revTPSS approximations. Error bars denote standard deviation calculated from these. Experimental values are from [52]**.**

Figures 5.1 and 5.2 demonstrate values of the lattice constants *a* and *c* respectively, when calculated for supercells with 25%, 50% and 75% of gallium. Dependence obtained by revTPSS technique for the pure material demonstrates stronger deviation from experimental

data in Figure 5.1. Small error bar shows insignificant dependence of lattice constant on atomic coordinates. Moreover, the obtained line shows nearly straight behavior.

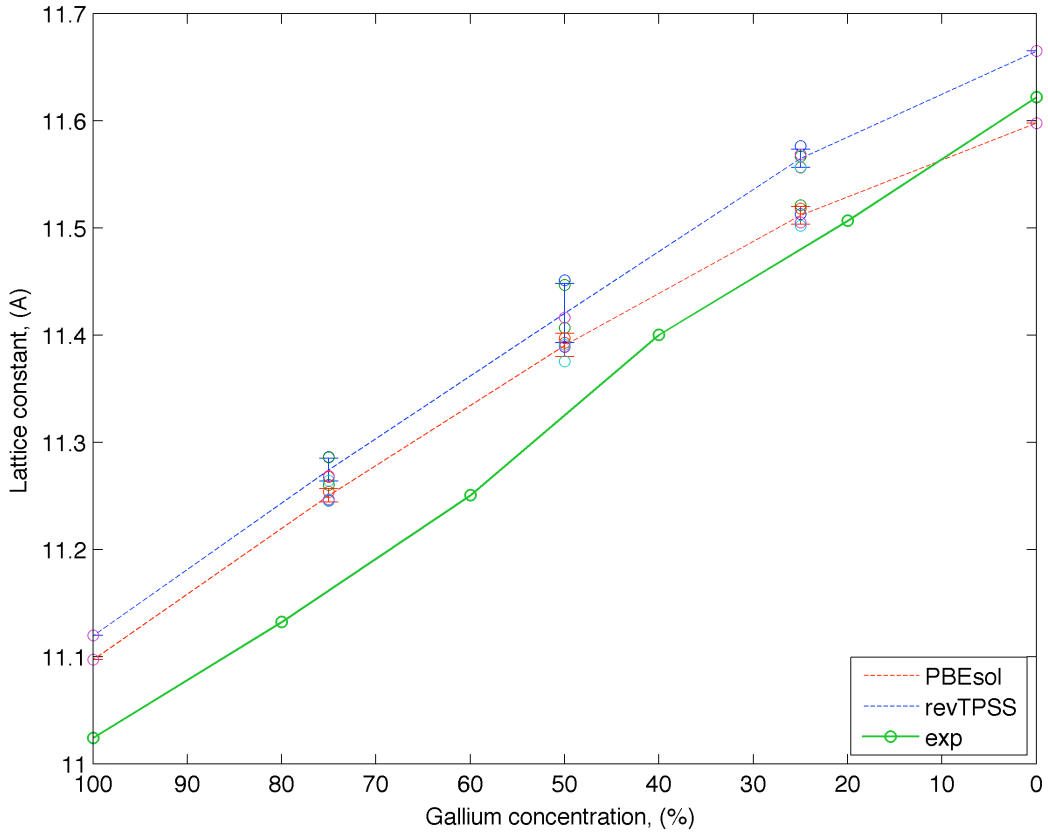

Figure 5.2 Dependence of lattice constant c on gallium concentration with different random atom positions (circles) obtained by PBEsol and revTPSS approximations. Experimental values are from [52].

We find a slight negative bending in our calculations in the indium rich side, which might also be present in the experimental data, but might also be an artifact due to uncertainties in the experimental values.

5.3. Dependence of the band gap on the c-parameter of mBJ functional

Tables below (Table 5.3) show the values of band gaps as the cmBJ-parameter is varied. Consequently, the parameter can be selected such that the calculated band gap matches the experimental values E_g for $CuGaSe_2$ and for $CuInSe_2$.

Table 5.3 Dependence of band gap on the cmBJ -parameter. The bold values denote the ones closest to the experimental band gaps

$CuGaSe_2$	
CMBJc	E_g, eV
1.2692	0.9874
1.3	1.0438
1.4	1.2242
1.5	1.3999
1.6	1.5712
1.62	1.605
1.63	1.6218
1.64	1.6385
1.665	**1.6802**
1.67	1.6885

$CuInSe_2$	
CMBJc	E_g, eV
1.2662	0.3768
1.3	0.4263
1.4	0.5684
1.5	0.7027
1.6	0.8286
1.7	0.9415
1.79	**1.0424**
1.8	1.0524

The use of the mBJ functional with the possibility of changing the cmBJ parameter gives flexibility in obtaining good band gaps. This parameter only affects the band structure features, since the lattice parameters are obtained using the revTPSS functional. Nevertheless, the cmBJ parameter is unique for each material, and thus requires a manual selection of the right value. However, as shown in the next section, in the case of alloys, averaging the c-parameter from the pristine material values yields good band gaps. Thus, the cmBJ parameter needs to be chosen only for the pristine systems.

5.4. The effect of alloying on the band gap

Figure 5.3 shows the dependence of the band gap on the gallium concentration for CIGS as calculated by different approximations. As it was mentioned above, in this work we employ the mBJ functional at the lattice constant optimized within the revTPSS structure.

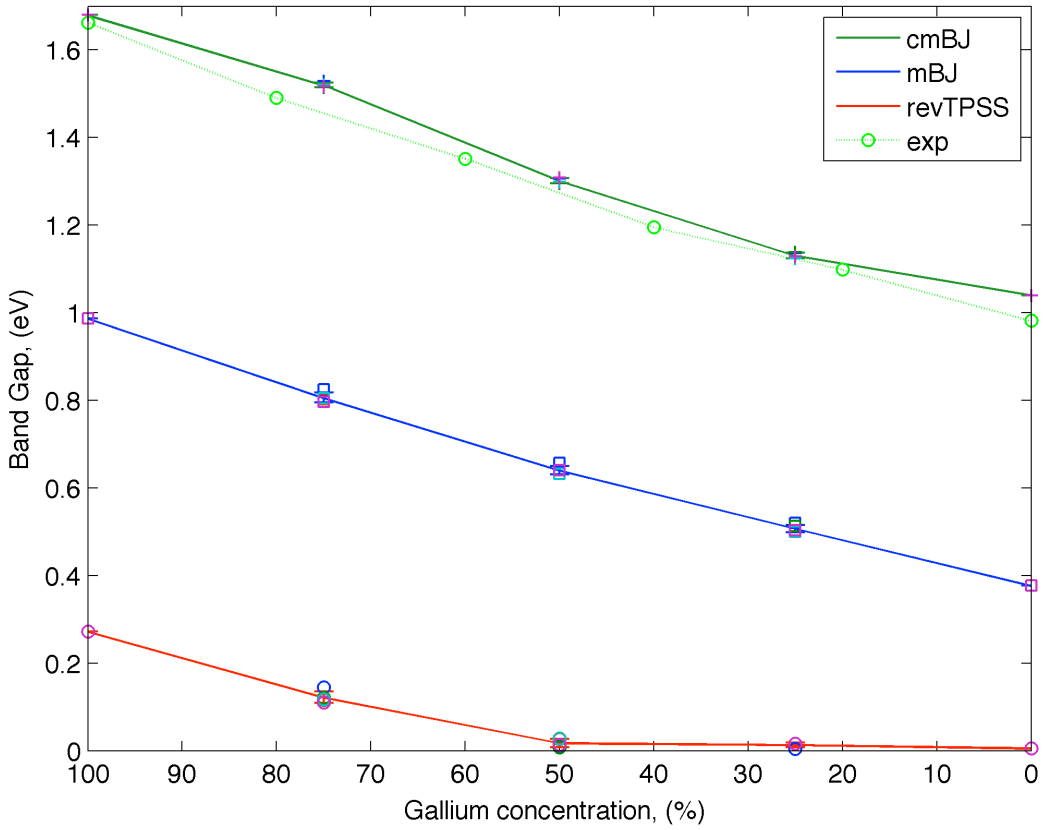

Figure 5.3 Influence of gallium concentration on band gaps as calculated using different approximations. Experimental values are from [52].

The cmBJ-parameter is choosen for each gallium concentration as the average between cmBJ for pure $CuInSe_2$ and $CuGaSe_2$ from the previous calculations (Table 5.3). It is evident from the graph that the band gap values obtained from the revTPSS method have a sharp fall and reach zero at about 50% of indium. All the used functionals result in a positive bending which matches the experimental line. The results obtained by the computational methods show that

the perfect band gap value (1.40 eV) can be obtained using CIGS materials with the 60% concentration of gallium.

SUMMARY

In this thesis, electronic and structural properties of $CuInSe_2$ and its alloys were investigated using first-principles DFT calculations. The work included a history study, an overview of the recent progress in solar cell technology, basics of photovoltaic physics, and fundamentals of the electronic structure theory. Lattice constants and band gaps of different chalcopyrite compounds were calculated using the GGA and meta-GGA methods with several functionals.

The first part of the calculations consisted of creation of 16 atoms unit cells, for which the full structural optimization was performed using VASP. Lattice constants were obtained by a number of different functionals such as LDA, PBE, PBEsol, AM05, and revTPSS. Further studies of the alloy properties were based on the PBEsol and revTPSS methods as they gave the best result for the lattice constant values of the pristine materials.

The theoretical study and the experimental data showed that CIGS is a good material for solar cells. Variation of the Ga-In substitution ratio changes the band gap of the CIGS absorber from around 1 eV to 2 eV, which can provide high efficiency solar devices. First, the band gaps were determined using the same methods as those for the lattice constants. However, most of them performed poorly. Regarding to the computational method based on the mBJ functional, errors were still 50% when using the self-consistent form, but it allowed improvement when the cmBJ parameter is tuned. The mBJ approximation with the properly chosen cmBJ parameter gave a good agreement with the available experimental values. Hence, our results showed that other more complex and much more expensive computational methods can be avoided. The band gap dependence on the gallium concentration was calculated from pure $CuInSe_2$ to pure $CuGaSe_2$ with 25% steps.

This work serves as a basis for several further investigations. One of the most interesting problems is the study of the band structures and comparison to the more accurate and computationally heavy methods such as the use of the hybrid functionals. We suggest that the meta-GGA based functionals, as presented in this thesis, should be useful to explain and interpret experimental observations for atomic-scale phenomena occurring in CIS. In particular, they can be used to study defect-related mechanisms that may sometimes remain out of reach in experiments.

6. REFERENCES

[1] S.-C. Chen, Y.-J. Chen, W. T. Chen, Y.-T. Yen, T.-S. Kao, T.-Y. Chuang, Y.-K. Liao, K.-H. Wu, A. Yabushita, T.-P. Hsieh, M. D. B. Charlton, D. P. Tsai, H.-C. Kuo, and Y.-L. Chueh, "Toward Omnidirectional Light Absorption by Plasmonic Effect for High Efficiency Flexible Non-Vacuum Cu(In,Ga)Se2 Thin Film Solar Cell.," *ACS Nano*, 2014.

[2] F. Dimroth, "New world record for solar cell efficiency at 46%. Press Release," *Presseinformation*, no. 26, pp. 1–4, 2014.

[3] B. Forge, "New best mark in thin-film solar performance with 21.7 percent efficiency. Press Release," *ZSW*, pp. 1–2, 2014.

[4] T. Maeda, T. Takeichi, and T. Wada, "Systematic studies on electronic structures of CuInSe2 and the other chalcopyrite related compounds by first principles calculations," *Phys. Status Solidi*, vol. 203, no. 11, pp. 2634–2638, 2006.

[5] N. Dombey, "The Nobel prize in physics," *Nature*, vol. 300, no. 5888, pp. 106–107, 1982.

[6] N. J. Murray Hill, "Vast power of the sun is tapped by battery using sand ingredient," *The New York Times*, New York Times, p. 1, 1954.

[7] G. Masson, M. Rekinger, I. T. Theologitis, and M. Papoytsi, "Global market outlook for PV 2013-2017," *Eur. Photovolt. Ind. Assoc.*, p. 6, 2013.

[8] Courtesy of National Renewable Energy Laboratory, "Champion laboratory cell efficiencies for different PV technologies." Golden, CO, 2014.

[9] S. O. Kasap, *Optoelectronics and photonics: principles and practices*. Pearson Education, 2001.

[10] M. D. Archer and M. A. Green, *Clean electricity from photovoltaics*, vol. 4, no. 2. London: Imperial College Press, 2015.

[11] M. J. Shiao, "Thin Film 2012 – 2016: Technologies , Markets and Strategies," 2012.

[12] M. J. Shiao and S. Moskowitz, "The global PV inverter landscape 2013: Technologies, Markets and Survivors," 2015.

[13] W. Mahdi, "Qatar to Tender 200 Megawatt of Solar-Power Projects in 2013," *Bloomberg*, vol. 3, p. 1, 2013.

[14] L. Zhu, R. F. Boehm, Y. Wang, C. Halford, and Y. Sun, "Water immersion cooling of PV cells in a high concentration system," *Sol. Energy Mater. Sol. Cells*, vol. 95, no. 2, pp. 538–545, 2011.

[15] A. Romeo, M. Terheggen, D. Abou-Ras, D. L. Bätzner, F.-J. Haug, M. Kälin, D. Rudmann, and A. N. Tiwari, "Development of thin-film Cu(In,Ga)Se2 and CdTe solar cells," *Prog. Photovoltaics Res. Appl.*, vol. 12, no. 23, pp. 93–111, 2004.

[16] P. Jackson, D. Hariskos, E. Lotter, S. Paetel, R. Wuerz, R. Menner, W. Wischmann, and M. Powalla, "New world record efficiency for Cu(In,Ga)Se2 thin-film solar cells beyond 20%," *Prog. Photovoltaics Res. Appl.*, vol. 19, pp. 894–897, 2011.

[17] D. L. Bätzner, A. Romeo, M. Terheggen, M. Döbeli, H. Zogg, and A. N. Tiwari, "Stability aspects in CdTe/CdS solar cells," in *Thin Solid Films*, 2004, vol. 451–452, pp. 536–543.

[18] M. Estela Calixto and A. Mendez-Blas, "Electrodeposited CuInSe2-Based Thin Films and Post-Deposition Treatments for Solar Cells: Feasibility to Use them in Space Applications," *Recent Prog. Sp. Technol. (Formerly Recent Patents Sp. Technol.*, vol. 4, no. 1, pp. 4–13, 2013.

[19] R. J. D. Tilley, *Defects in Solids*. 2008.

[20] L. E. Oikkonen, M. G. Ganchenkova, A. P. Seitsonen, and R. M. Nieminen, "Formation, migration, and clustering of point defects in CuInSe 2 from first principles," *J. Phys. Condens. Matter*, vol. 26, no. 34, p. 345501, 2014.

[21] L. E. Oikkonen, M. G. Ganchenkova, A. P. Seitsonen, and R. M. Nieminen, "Vacancies in CuInSe2: new insights from hybrid-functional calculations," *Journal of Physics: Condensed Matter*, vol. 23, no. 42. p. 422202, 2011.

[22] L. E. Oikkonen, M. G. Ganchenkova, A. P. Seitsonen, and R. M. Nieminen, "Redirecting focus in CuInSe 2 research towards selenium-related defects," *Phys. Rev. B - Condens. Matter Mater. Phys.*, vol. 86, no. 16, pp. 1–5, 2012.

[23] L. E. Oikkonen, M. G. Ganchenkova, A. P. Seitsonen, and R. M. Nieminen, "Effect of sodium incorporation into CuInSe2 from first principles," *J. Appl. Phys.*, vol. 114, no. 8, 2013.

[24] L. E. Oikkonen, M. G. Ganchenkova, A. P. Seitsonen, and R. M. Nieminen, "Mass transport in CuInSe2 from first principles," *J. Appl. Phys.*, vol. 113, no. 13, 2013.

[25] A. Chirilă, P. Reinhard, F. Pianezzi, P. Bloesch, A. R. Uhl, C. Fella, L. Kranz, D. Keller, C. Gretener, H. Hagendorfer, D. Jaeger, R. Erni, S. Nishiwaki, S. Buecheler, and

A. N. Tiwari, “Potassium-induced surface modification of Cu(In,Ga)Se2 thin films for high-efficiency solar cells.,” *Nat. Mater.*, vol. 12, no. December, pp. 1107–11, 2013.

[26] S. Siebentritt, M. Igalson, C. Persson, and S. Lany, “The electronic structure of chalcopyrites-bands, point defects and grain boundaries,” *Prog. Photovoltaics Res. Appl.*, vol. 18, pp. 390–410, 2010.

[27] J. Harris, C. Newman, O. Masala, L. Wylde, and N. Pickett, “Copper-Indium-Gallium-Chalcogenide Nanoparticle Precursors for Thin-Film Solar Cells,” 04-Sep-2014.

[28] R. M. Martin, *Electronic Structure: Basic Theory and Practical Methods*. 2004.

[29] L. Oikkonen, “Atomic-scale defects in solar cell material CuInSe2 from hybrid-functional calculations,” Aalto University, 2013.

[30] P. Hohenberg and W. Kohn, “Inhomogeneous Electron Gas,” *Phys. Rev.*, vol. 136, no. 5, pp. 1912–1919, 1964.

[31] U. Von Barth and L. Hedin, “A local exchange-correlation potential for the spin polarized case. i,” *J. Phys. C Solid State Phys.*, vol. 5, no. 13, pp. 1629–1642, 2001.

[32] W. Kohn and L. J. Sham, “Self-consistent equations including exchange and correlation effects,” *Phys. Rev.*, vol. 140, no. 4A, 1965.

[33] E. S. Kryachko and E. V. Ludeña, “Density functional theory: Foundations reviewed,” *Physics Reports*, 2014.

[34] W. Kohn, “Nobel Lecture: Electronic structure of matter—wave functions and density functionals,” *Reviews of Modern Physics*, vol. 71, no. 5. pp. 1253–1266, 1999.

[35] J. Perdew, K. Burke, and M. Ernzerhof, “Generalized Gradient Approximation Made Simple.,” *Phys. Rev. Lett.*, vol. 77, no. 18, pp. 3865–3868, 1996.

[36] A. E. Mattsson, R. Armiento, J. Paier, G. Kresse, J. M. Wills, and T. R. Mattsson, “The AM05 density functional applied to solids,” *J. Chem. Phys.*, vol. 128, no. 8, 2008.

[37] J. P. Perdew, A. Ruzsinszky, G. I. Csonka, O. a. Vydrov, G. E. Scuseria, L. a. Constantin, X. Zhou, and K. Burke, “Generalized gradient approximation for solids and their surfaces,” vol. 136406, no. April, pp. 1–4, 2007.

[38] C. J. Cramer, *Essentials of Computational Chemistry Theories and Models*, vol. 42, no. 2. 2004.

[39] J. Sun, M. Marsman, G. I. Csonka, A. Ruzsinszky, P. Hao, Y. S. Kim, G. Kresse, and J. P. Perdew, “Self-consistent meta-generalized gradient approximation within the

projector-augmented-wave method," *Phys. Rev. B - Condens. Matter Mater. Phys.*, vol. 84, no. 3, pp. 1–12, 2011.

[40] F. Tran and P. Blaha, "Accurate band gaps of semiconductors and insulators with a semilocal exchange-correlation potential," *Phys. Rev. Lett.*, vol. 102, no. 22, pp. 5–8, 2009.

[41] P. Mori-Sánchez, A. J. Cohen, and W. Yang, "Localization and delocalization errors in density functional theory and implications for band-gap prediction," *Phys. Rev. Lett.*, vol. 100, no. 14, 2008.

[42] S. Kümmel and L. Kronik, "Orbital-dependent density functionals: Theory and applications," *Rev. Mod. Phys.*, vol. 80, no. 1, pp. 3–60, 2008.

[43] A. D. Becke, "A new mixing of Hartree–Fock and local density-functional theories," *J. Chem. Phys.*, vol. 98, no. 2, p. 1372, 1993.

[44] J. Heyd, G. E. Scuseria, and M. Ernzerhof, "Hybrid functionals based on a screened Coulomb potential," *J. Chem. Phys.*, vol. 118, no. 18, pp. 8207–8215, 2003.

[45] J. Pokluda, M. Černý, M. Šob, and Y. Umeno, "Ab Initio calculations of mechanical properties: Methods and applications," *Prog. Mater. Sci.*, 2015.

[46] E. Parthé, *Crystal Chemistry of Tetrahedral Structures*. London: CRC Press, 1964.

[47] A. Neisser, "Gallium as an Isovalent Substitution in CuInS2 Absorber layers for Photovoltaic Applications," Freie Universität Berlin, 2001.

[48] A. R. Denton and N. W. Ashcroft, "Vegards law," *Phys. Rev. A*, vol. 43, no. 6, pp. 3161–3164, 1991.

[49] A. D. Becke, "Current-density dependent exchange-correlation functionals," *Canadian Journal of Chemistry*, vol. 74, no. 6. pp. 995–997, 1996.

[50] J. F. Georg Kresse, Martijn Marsman, *Vienna Ab-initio Simulation Package (VASP) the Guide*. 2014.

[51] Y. S. Kim, M. Marsman, G. Kresse, F. Tran, and P. Blaha, "Towards efficient band structure and effective mass calculations for III-V direct band-gap semiconductors," *Phys. Rev. B - Condens. Matter Mater. Phys.*, vol. 82, no. 20, 2010.

[52] V. G. Lifshits, K. Oura, A. A. Saranin, and A. V. Zotov, "Landolt-Börnstein - Group III Condensed Matter," in *Adsorbed Layers on Surfaces. Part 1: Adsorption on Surfaces and Surface Diffusion of Adsorbates*, 2001, pp. 259–419.

[53] V. Shaposhnikov, A. Krivosheeva, V. Borisenko, J.-L. Lazzari, and F. D'Avitaya, "Ab initio modeling of the structural, electronic, and optical properties of A(II)B(IV)C(V)2 semiconductors," *Phys. Rev. B*, vol. 85, no. 20, pp. 1–9, 2012.